

Accelerated Development of Multi-component Alloys in Discrete Design Space Using Bayesian Multi-Objective Optimization

Osman Mamun¹, Markus Bause², and Bhuiyan Shameem Mahmood Ebna Hai^{1,2,*}

¹Fehrmann MaterialsX GmbH - Fehrmann Tech Group, Hamburg, Germany

²Helmut Schmidt University - University of the Federal Armed Forces Hamburg, Germany

*Corresponding author: shameem.ebna.hai@fehrmann-materials.com

ABSTRACT

Bayesian optimization (BO) protocol based on Active Learning (AL) principles has garnered significant attention due to its ability to optimize black-box objective functions efficiently. This capability is a prerequisite for guiding autonomous and high-throughput materials design and discovery processes. However, its application in materials science, particularly for novel alloy designs with multiple targeted properties, remains limited. This limitation is due to the computational complexity and the lack of reliable and robust acquisition functions for multiobjective optimization. In recent years, expected hypervolume-based geometrical acquisition functions have demonstrated superior performance and speed compared to other multiobjective optimization algorithms, such as Thompson Sampling Efficient Multiobjective Optimization (TSEMO), Pareto Efficient Global Optimization (parEGO), etc. This work compares several state-of-the-art multiobjective BO acquisition functions, i.e., parallel expected hypervolume improvement (qEHVI), noisy parallel expected hypervolume improvement (qNEHVI), parallel Pareto efficient global optimization (parEGO), and parallel noisy Pareto efficient global optimization (qNparEGO) for the multiobjective optimization of physical properties in multi-component alloys. We demonstrate the impressive performance of the qEHVI acquisition function in finding the optimum Pareto front in 1-, 2-, and 3-objective Aluminium alloy optimization problems within a limited evaluation budget

and reasonable computational cost. In addition, we discuss the role of different surrogate model optimization methods from a computational cost and efficiency perspective. Finally, we illustrate the efficiency of the pool-based active learning protocol to further accelerate the discovery process by conducting several computational and experimental campaigns in each iteration. This approach is particularly advantageous for use in massively parallel high-throughput synthesis facilities and computer architectures.

INTRODUCTION

In materials science, when designing suitable materials for a specific application from a broad range of alternatives, a researcher must consider factors such as individual characteristics, applications, advantages, and limitations. A lack of understanding of the functional requirements and the specific design criteria that must be met can lead to the development of sub-optimal materials. In turn, the lack of proper optimization can result in significant costs or wasted investment, leading to premature component or product failure. For example, gas turbine engines must operate at high temperatures withstanding high pressures to achieve high efficiency. This extreme condition not only improves the thermal efficiency of the process but also benefits the environment by helping to reduce carbon emissions [Long et al. \(2018\)](#). Austenitic stainless steel and Ni-based superalloys are widely used in gas turbines due to their excellent corrosion resistance and high yield and tensile strength at elevated temperatures and pressures [Mamun et al. \(2021\)](#). However, robust corrosion resistance and high strength are not the only criteria to be met; an ideal material for gas turbine engines should also have low density, high thermal conductivity, and a small coefficient of linear thermal expansion [Khatamsaz et al. \(2023\)](#). Likewise, in the design of a multi-principal-element alloy (MPEA), several objectives must be fulfilled, including low-density, high-temperature yield strength, creep resistance, and oxidation resistance [Liu et al. \(2023\)](#).

Designing complex materials with desired properties requires expensive computational modeling, such as density functional theory (DFT) computations, thermochemical simulations, molecular dynamics calculations, and extensive experimental campaigns. The highly non-linear interactions between design variables and target properties mean that high-fidelity models often behave like

black-box functions. This behavior hinders the ability to design tailored materials, which usually necessitates carrying out these costly computations or experiments for a wide range of candidate materials to optimize several competing properties. A combinatorial approach to such problems involves conducting simulations or experiments on an exhaustive combination of numerous variables, including compositions, processing, and synthesis parameters. This approach aims to establish a structure-property relationship that can guide scientists in understanding the interplay of different parameters [Gebhardt et al. \(2012\)](#), potentially leading to the development of state-of-the-art novel materials. However, this method needs more scalability and is time-consuming [Cantor \(2014\)](#). Estimates suggest it can take a few decades to productionize novel materials from the ideation phase to the market [Agrawal and Choudhary \(2016\)](#). Autonomous experimental systems have emerged as powerful tools to expedite the lab-to-market process. These systems function as oracles, suggesting the following experiment to be performed sequentially, thereby avoiding the combinatorial approach and saving time and resources.

Autonomous experimental and computational systems are becoming the frontier of accelerated materials design [Liang et al. \(2021\)](#). In this context, active learning has emerged as a revolutionary tool, significantly contributing to discovering novel materials while minimizing experimental and computational costs. The primary advantage of active learning is its ability to iteratively guide the selection of experiments toward a target design objective, thus reducing the number of required experiments. Bayesian optimization, a class of active learning methods, employs a surrogate model and a utility function to recommend the subsequent experiment or computation [Snoek et al. \(2012\)](#). This surrogate model correlates design variables, such as materials composition, with target properties. The utility function then quantifies the impact of various unknown parameters on these target properties, guiding the selection of the following experiment(s) to maximize the utility function's value. Bayesian optimization offers several advantages in experimental design, including sample efficiency, global optimization, and the ability to handle complex objective functions without a closed form [Shahriari et al. \(2016\)](#). As a result, Bayesian optimization (BO) has become an increasingly attractive choice for accelerating materials research and optimizing

material properties beyond current state-of-the-art technologies, as evidenced by the plethora of publications involving the application of BO in materials science.

Although Bayesian optimization (BO) has demonstrated promising outcomes in the materials science field, its implementation is still restricted due to several factors:

- (a) It is primarily employed for single-objective optimization.
- (b) Only a single experiment or computational recommendation is feasible in each iteration, which constrains the application of parallel computation or experimentation strategies for improved data collection.
- (c) Surrogate probabilistic modeling often proves expensive and impractical in contemporary computer architectures. For instance, the Gaussian Process, a common choice for surrogate modeling, scales as N^3 , where N represents the number of data instances.

Single-objective optimization can be achieved using acquisition functions such as the Upper Confidence Bound (UCB), Lower Confidence Bound (LCB), Expected Improvement (EI), and Probability of Improvement (PI) [Frazier \(2018\)](#). However, multiobjective optimization, which involves simultaneously optimizing several competing properties, adding a layer of complexity. To address this, several approaches have been proposed. For instance, Thompson Sampling for Efficient Multiobjective Optimisation (TSEMO), a multiobjective evolutionary algorithm [Bradford et al. \(2018\)](#); Pareto Efficient Global Optimization (parEGO), extending the expected improvement acquisition function to multi-dimensional problems [Knowles \(2006\)](#); and Expected Hypervolume Improvement (EHVI), a hypervolume maximization algorithm [Hupkens et al. \(2015\)](#). Among these, EHVI has gained significant attention due to its simplicity and effectiveness. This method aims to maximize the hypervolume covered by the non-dominated points relative to a fixed reference point, effectively identifying a well-defined Pareto front.

However, like TSEMO and parEGO, EHVI is notoriously costly and does not support parallel computations. The parallel expected hypervolume improvement (qEHVI) and parallel noisy expected hypervolume improvement methods overcome these limitations by enabling the parallel

calculation of the hypervolume for different points using the inclusion-exclusion principle [Daulton et al. \(2020\)](#). Similarly, the parallel parEGO and its noisy variant parallelize the scalarization process, thereby enabling Bayesian optimization for multi-dimensional problems. Having access to these acquisition functions for multiobjective optimization, the question naturally arises of how to select the best algorithm for the application of novel materials design and discovery. Specifically, there are two important factors to consider: 1. the surrogate model construction, and 2. the acquisition function selection.

Another challenge in Bayesian Optimization (BO) within materials science is the common practice of making only a single recommendation per iteration, which is inefficient when multiple parallel experiments or computations are possible. To address this, several strategies have been suggested, such as dividing the objective space into clusters based on similarity or distance vectors to maximize data diversity and informativeness [Mamun et al. \(2022\)](#); [Zhan et al. \(2021\)](#). The qEHVI also supports the generation of multiple candidate points simultaneously, ensuring proper propagation of uncertainty.

This work presents a Bayesian optimization (BO) framework to efficiently optimize multiple properties simultaneously for Aluminium alloy design problems. First, we compare the performance of two ways of constructing or conditioning the surrogate model on the training data: maximum likelihood estimation and Monte Carlo simulation. Our analysis shows that maximum likelihood estimation provides the best trade-off for accuracy and time constraints. Then, we compare three different acquisition functions for 1-dimensional properties optimization, i.e., probability of improvement (PI), expected improvement (EI), and expected hypervolume improvement (EHVI). Our results illustrate that all three acquisition functions perform more or less similarly and vastly outperform the random data acquisition algorithm, with PI being slightly worse than the other two algorithms. Next, we investigate the performance of four different acquisition functions for multi-dimensional optimization problems, i.e., expected hypervolume improvement (EHVI), noisy expected hypervolume improvement (NEHVI), Pareto efficient global optimization (parEGO) and noisy Pareto efficient global optimization (NparEGO). Except for parEGO, the remaining three

algorithms outclasses the random data acquisition algorithm. However, when considering the computational cost of computing the utility value with the noisy variant of these algorithms, qEHVI becomes an automatic choice for multi-dimensional problems; however, for noisy data (e.g., experimental observations), qNEHVI should be preferred to deal with the observation uncertainty. We also demonstrate that the EHVI can identify the global Pareto front with only a 70-75 evaluation budget and achieves a hypervolume that is over 90% of the maximum achievable value. Finally, we demonstrate that multiple data acquisition in each iteration cycle can lead to enhanced performance, in terms of time to reach a predefined hypervolume, ultimately leading to faster alloy design and discovery.

METHODS

In this work, we present an active learning framework for the multi-objective optimization of Aluminium alloy design and discovery. Below, we briefly describe the underlying theory of the active learning framework, including surrogate model construction and various single- and multi-objective acquisition functions.

Figure 1 illustrates the general workflow of the active learning cycle. The cycle begins with observed data for 'n' cases, featuring variables $\{F_1, F_2, \dots, F_n\}$ and targets $\{T_1, T_2, \dots, T_n\}$. To simulate a realistic situation, we start with a fixed number of initial points (e.g., 25, 50, etc.) acquired at random. The initial seed points then undergo a data preparation stage where:

- (a) For experimental data, data instances where elongation is greater than 60% are removed as they might contain experimental measurement errors. Since our objective is to minimize the elongation in most of the realistic scenarios, this data processing will have no significant impact on the model bias.
- (b) Any feature with null values is removed, and
- (c) The data is scaled between zero and one to remove numerical scale bias.

A probabilistic model is subsequently trained on these data points, enabling the inference of data instances where only the feature vector is known. In multi-objective optimization, either a

single model can be used to model the joint probability distribution of the target properties or separate models can be trained for each target. Based on the model's inferences for both single- and multi-objective problems, the utility value is computed using acquisition functions for the discrete data instances for which the features are known but the target properties are not. The algorithm then selects the point or points (in cases where several candidates are chosen in each iteration) that maximize the utility function. These recommended points are then added to the existing training database. The cycle continues until it reaches the optimum point. For single-objective optimization, the minimum or maximum value is considered the optimum and used as the stopping criterion. For multi-objective optimization, the stopping criterion is the hypervolume covered by the non-dominated points in the entire database. In situations where the global maximum hypervolume is not known a priori, the cycle can continue until it reaches a predetermined number of iterations or a specified hypervolume that meets specific design criteria.

Based on the above discussion, we can identify two key components in an active learning cycle:

- (a) A probabilistic model, serving as a surrogate model, to approximate the underlying data-generating function. In this article, we use Gaussian processes, which are particularly effective in multi-objective optimization.
- (b) An acquisition function is used to quantify the utility of all the candidate data points, which then guides the selection of the next data point to evaluate.

Gaussian Process

The Gaussian process (GP), a powerful non-parametric machine learning algorithm, has become the workhorse in Bayesian optimization due to its flexibility and excellent uncertainty quantification capability. To estimate the mean $\hat{\mu}(x^*)$ and standard deviation $\hat{\sigma}(x^*)$ of an unobserved data point x^* , the Gaussian process is employed. It defines the joint distribution of the observed and unobserved objective values as follows:

$$\begin{bmatrix} \mathbf{y} \\ y_* \end{bmatrix} \sim \mathcal{N}\left(0, \begin{bmatrix} K + \sigma^2 I & K_*^T \\ K_* & K_{**} \end{bmatrix}\right) \quad (1)$$

where \mathbf{y} represents the observed values, y_* the unobserved values, and K , K_* , and K_{**} are components of the kernel matrix. Specifically, $K + \sigma^2 I$ is the covariance matrix of the observed observations, K_*^T and K_* represent the covariances between observed and unobserved observations, and K_{**} is the covariance matrix of the unobserved observations.

In this article, we utilise the Matérn 5/2 kernel function, a widely employed kernel function renowned for its useful mathematical properties. The Matérn 5/2 kernel for two points p and q in the design space is defined as:

$$k(\mathbf{p}_j, \mathbf{q}_j) = \sigma_0^2 \cdot \left(1 + \frac{\sqrt{5}r}{l_j} + \frac{5r^2}{3l_j^2}\right) \exp\left(-\frac{\sqrt{5}r}{l_j}\right) \quad (2)$$

where $r = \sqrt{(p_j - q_j)^2}$ and l is the characteristic length.

The mean and variance of the posterior are computed as follows:

$$\hat{\mu}(\mathbf{x}) = y_* = K_* [K + \sigma^2 I]^{-1} \mathbf{y} \quad (3)$$

and

$$\text{cov}(y_*) = K_{**} - K_* [K + \sigma^2 I]^{-1} K_*^T \quad (4)$$

To make inferences on unknown design features, we utilize two methods:

- (a) Maximum a Posteriori (MAP), which formulates the GP problem as an optimization problem with respect to the target density, resulting in faster model training and inference compared to No U-Turn Samplers (NUTS).
- (b) No U-Turn Samplers (NUTS), a full Monte-Carlo method that updates the posterior via an acceptance-rejection algorithm, making model training and inference more resource-

intensive.

For MAP training, we utilized two different open source implementations:

- (a) scikit-learn, more commonly known as sklearn. We used the sklearn’s *GaussianProcessRegressor* API to train the model. Since sklearn’s model API is not compatible with the BoTorch acquisition function API (which we used to implement all the acquisition functions in this study), we provide a custom wrapper to make the sklearn model compatible with the BoTorch acquisition function API.
- (b) BoTorch’s native *SingleTaskGP* model API along with *ModelList* API for multiobjective model training.

Apart from using the aforementioned two models, we also used sparse axis-aligned subspace GP (SAASGP), which, unlike predefined inflexible kernels, utilizes a flexible kernel definition to systematically reduce the number of parameters to train while capturing the anisotropic nature of the feature space.

For a large number of dimensions, Gaussian Processes (GP) scale as N^3 and become computationally very expensive, particularly when assuming a certain degree of smoothness. To enhance the sample efficiency of GP, several assumptions are made in the Sparse Axis-Aligned Subspaces (SAAS) GP formulation [Eriksson and Jankowiak \(2021\)](#):

- (a) Assume a hierarchy of feature relevance to reduce the number of active features systematically.
- (b) Incorporate a flexible class of smooth, non-linear functions.
- (c) Ensure tractable inference due to the differentiable nature of the kernel functions.

To facilitate the assumptions mentioned above in Sparse Axis Aligned Subspaces (SAAS), the Gaussian Process (GP) models are initialized with a structured prior over the kernel hyperparameters. These include:

- (a) A weak prior over the kernel variance.
- (b) A half-Cauchy prior on the global shrinkage or regularization parameter, leading to the zeroing out of irrelevant features.
- (c) A half-Cauchy prior on the (inverse squared) length scale for Radial Basis Function (RBF) or Matern kernels.

Due to these modifications, most dimensions are effectively switched off (their contributions become negligible or zero) in line with Automatic Relevance Determination (ARD). The half-Cauchy prior over the length scale causes these values to cluster around zero unless the data provides sufficient evidence to increase them. By design, the model remains parsimonious; however, as more data is gathered, some model parameters may deviate from zero, resulting in an excellently regularized model. The SAASGP models are trained with Monte-Carlo integration along with No U-turn samplers (NUTS).

Acquisition Functions

Probability of Improvement (PI)

If we denote the f^* to be the maximum obtained so far in the context of a maximization problem, while $\Phi(\cdot)$ and $\phi(\cdot)$ represent the normal cumulative distribution function (CDF) and the probability density function (PDF), respectively, of the standard normal random variable. Then, the probability of improvement over the current best point is defined as:

$$PI(x) = P(f(x) \geq f(x^*)) = \Phi\left(\frac{\mu(x) - f(x^*)}{\sigma(x)}\right) \quad (5)$$

Here, PI is the probability of finding a better function value at position x than the current best value ($f(x^*)$). In simple terms, whenever a point x offers an improvement over the current best point; it is given a reward (or utility function value); otherwise no reward at all. Then, the probability of improvement is computed as the expected utility. In this work, we use the parallel implementation of the PI acquisition function, which will be dubbed qPI in the rest of the article.

Expected Improvement (EI)

The probability of improvement acquisition function has a serious flaw in that it only considers the function value at position x that is better than the current best point, irrespective of the magnitude of the improvement, which leads to suboptimal performance as the algorithm often gets trapped in a local optima. To overcome this limitation, expected improvement (EI) was proposed, which not only takes the improvement over the current best into account, also the magnitude of the improvement is taken into account to distinguish the global optimum from the local optimums. EI is computed as:

$$EI(x) = \mathbb{E}[\max(0, f^* - f(x))] = (f^* - \mu(x))\Phi\left(\frac{f^* - \mu(x)}{\sigma(x)}\right) + \sigma(x)\phi\left(\frac{f^* - \mu(x)}{\sigma(x)}\right) \quad (6)$$

where \mathbb{E} denotes the expectation value, Φ and ϕ are the Gaussian CDF and PDF, respectively. In this article, we used the parallel implementation of the EI acquisition function, which shall be referred to as qEI in the subsequent analysis.

Expected Hypervolume Improvement (EHVI)

For a given Pareto front, denoted as \mathcal{P} , the hypervolume (HV) is defined as the d-dimensional Lebesgue measure of the corresponding subspace. In our multi-objective optimization approach, we utilized the expected hypervolume improvement as the acquisition function for the active learning cycle. For a Pareto set \mathcal{P} and a reference point r , the hypervolume improvement of a vector y is defined as:

$$HVI(\mathcal{P}, y) = HV(\mathcal{P} \cup \{y\}) - HV(\mathcal{P}). \quad (7)$$

The expected hypervolume is the expectation of the HVI over the posterior distribution, which can be estimated using the Monte Carlo integration.

$$\alpha_{EHVI(x|\mathcal{P})} = \mathbb{E}[HVI(f(x)|\mathcal{P})] \quad (8)$$

In this work, we used The q-expected hypervolume improvement (qEHVI), a parallel implementation of the EHVI algorithm developed by Facebook [Daulton et al. \(2020\)](#), which introduces several modifications for practical implementation. Unlike the original EHVI, which utilizes gradient-free acquisition function optimization, qEHVI leverages auto-differentiation to facilitate the optimization of the acquisition function using first-order and quasi-second-order methods. Additionally, it enables the computation of EHVI on modern parallel computing architectures, significantly increasing speed and efficiency. Owing to these significant improvements, qEHVI outperformed other multi-objective Bayesian optimization algorithms in many standard benchmark problems.

Noisy Expected Hypervolume Improvement (NEHVI)

In the EHVI or qEHVI algorithm, one of the major assumptions is that the observations are noise-free; unfortunately, in many real-world applications, this assumption seriously challenges the performance of the qEHVI for efficient Bayesian optimization. Instead of using only the posterior mean to compute the expected hypervolume improvement of different candidate points, the posterior uncertainty is also taken into account to compute the acquisition function values. The acquisition function, noisy expected hypervolume improvement (NEHVI) is defined as:

$$\alpha_{NEHVI(x)} = \int \alpha_{EHVI}(x|\mathcal{P}_n)p(f|D_n)df \quad (9)$$

where P_n denotes the Pareto frontier over $f(X_n)$. Using MC integration, the inner expectation of $\alpha_{NEHVI(x)}$ is computed. The parallel version of this algorithm is dubbed as qNEHVI [Daulton et al. \(2021\)](#).

Pareto Efficient Global Optimization (parEGO)

Pareto Efficient Global Optimization (parEGO) is a multiobjective optimization algorithm where the multiobjective optimization problem is transformed into a single objective optimization problem using a suitable scalarization algorithm. Then it applies the expected improvement (EI) acquisition function (described above) to compute the utility of candidate points. For parEGO algorithm, the random augmented Chebyshev scalarizations technique is used [Knowles \(2006\)](#).

BoTorch implemented a novel parallel version of this algorithm, qparEGO, which is used in this article.

Noisy Pareto Efficient Global Optimization (NparEGO)

Similar to the qNEHVI algorithm discussed above, the noisy variant of the parEGO (dubbed as NparEGO) utilizes the posterior mean and standard deviation to compute the true Pareto frontier. In this article, we also use the parallel version of this algorithm, known as qNparEGO.

Multiple Data Acquisition

There are several ways to acquire multiple data in each iteration. In this article, we use the sequential greedy batch selection algorithm as implemented in the BoTorch code. In a sequential greedy batch selection algorithm, the utility values of all the candidate points are evaluated first, and then the best candidate point is selected. Then, for subsequent candidate selection, the previously selected candidates are held constant to compute the utility values of the remaining candidate points.

RESULTS AND DISCUSSION

Dataset

In this study, two different datasets were utilized:

- (a) Computational Dataset: This dataset was exclusively generated using CALPHAD simulation software for this study. It comprises 13,700 data instances with 41 features (after preprocessing steps). Detailed information regarding the simulation protocol and dataset properties are provided in Appendix A of the Supporting Information.
- (b) Experimental Dataset: This data was gathered and compiled into a consistent and reliable dataset by peer-reviewed literature Pfeiffer et al. (2022) and Fehrmann MaterialsX GmbH. It includes data from experiments conducted in-house and other credible sources, such as published articles and a European consortium. The dataset comprises approximately 3,700 data instances with 13 features (after preprocessing steps), collected over several years. These features cover the composition of elements and processing parameters like temper

and temperature. Detailed information on the dataset properties is illustrated in Appendix B of the Supporting Information.

Surrogate Model Construction

For surrogate model training, we used BoTorch’s [Balandat et al. \(2020\)](#) *SingleTaskGP* model API (BT-MLE) and scikit learn’s [Pedregosa et al. \(2011\)](#) *GaussianProcessRegressor* API (SK-MLE). As for the kernel, we used a combination of Matern kernel along with a linear kernel. For optimization of both the models, we used scipy’s [Virtanen et al. \(2020\)](#) optimizer module. For SAASGP model training, we used BoTorch’s *SaasFullyBayesianSingleTaskGP* model API. To train the model, we used the GPyTorch’s [Gardner et al. \(2018\)](#) NUTS sampler (MC-NUTS).

From a computational standpoint, SAASGP is more resource-intensive than both BT-MLE and SK-MLE. However, SAASGP tends to yield a more accurate model, particularly in scenarios with limited data. For active learning workflow, it is crucial to have a reliable surrogate model construction algorithm to faithfully model the underlying solution surface, at least qualitatively, for optimization purposes. In order to quantify the effectiveness of these aforementioned three model implementations to favor the best model (i.e., BT-MLE, SK-MLE, and SAASGP), we focus on the following metrics:

- (a) Correlation coefficient (R^2) on the holdout test dataset.
- (b) Coverage of the model, meaning how many actual values lie within the two standard deviations of the predicted values.
- (c) Relative computational cost to train the model.

The higher the R^2 , the better the model predicts the underlying solution surface. Similarly, from an uncertainty quantification perspective, a well-calibrated model should have coverage that is close to 95%. Despite significant improvements in computer hardware and software, still the computational cost is a major hindrance to apply Bayesian optimization to large-scale scientific problems. In figure 2, we summarize the relative performance of these three implementations. The models are trained five times with random 1500 data and tested on the rest of the data.

In our investigation, we found that the BT-MLE implementation performed consistently poorly compared to the other two implementations. Interestingly, SK-MLE performed as well as SAASGP, if not better, for our purpose. Even though for some tasks, the R^2 is not as high as we would expect, we still found them to be excellent for Bayesian optimization as the model can predict the relative values quite faithfully, as evidenced by the coverage. Coverage for both SK-MLE and SAASGP ranges around 90% - 95%, which qualifies both to be very well-calibrated uncertainty quantification techniques. However, if we observe the relative time to train the models, SK-MLE becomes an automatic choice over the SAASGP. Considering the R^2 values, coverage, and time, we used SK-MLE in our subsequent analysis. However, SAASGP can be a powerful GP model for specific material science problems, where the MAP-based model performs unsatisfactorily.

1-Dimensional Properties Optimization Results

In Figure 3, we present the optimization profile for various targets in the computational dataset for 1-dimensional optimization problems. Bayesian optimization showed impressive performance for density optimization in finding the optimum point (in this case, the minimum) by all three acquisition functions, i.e., qEI, qPI, and qEHVI. Across all five runs, with twenty-five seed points, the algorithm consistently reached the global minimum (i.e., 1.4 g.cm^{-3}) in less than 20 iterations. This indicates that to find the minimum point in a dataset of more than 13,000 data points, Bayesian optimization requires fewer than 50 computations. In comparison, random data acquisition could not reach the global minimum even once in the five trial simulated runs.

For heat capacity optimization, the performance is similarly impressive in finding the maximum, reaching it within 25 iterations for all five runs, in stark contrast to the poor performance of random data acquisition. In the case of thermal conductivity, the average number of iterations to reach the global maximum is about 40-50 for all three Bayesian optimization algorithms; however, random data acquisition also performed similarly well for this problem, owing to the fact that the data distribution is narrower and right-skewed (see supporting information) it is easier to find materials that are close to the global maximum. For electric conductivity, both qEI and qPI performed slightly better than the qEHVI. In this instance, the performance of random acquisition was also

similar to that of Bayesian optimization.

These results highlight that the success of Bayesian optimization also depends on the underlying data behavior. In scenarios with noise, a broad distribution of the target property, or non-representative features, the performance of Bayesian optimization may be less satisfactory. Effective application of Bayesian optimization in realistic situations still greatly benefits from domain knowledge, especially in designing the features or the surrogate model that can make reliable predictions on unknown observations. From the one-dimensional optimization of the computational data, we can conclude that the traditional single-objective acquisition function is better suited for one-dimensional optimization than the multiobjective acquisition function, such as qEHVI.

In Figure 4, we present the optimization profile for the experimental dataset across various target properties, i.e., yield strength, ultimate tensile strength, and elongation. The yield strength reaches its global maximum (559 MPa) within 40 to 50 iterations for qEI and qEHVI but settles at a local maximum (552 MPa) for qPI. Regarding ultimate tensile strength, most trials achieve the global maximum within 20 to 60 iterations for qEI and qEHVI, except for qPI, which reaches the global optimum on average at the 100th iteration. All trials reach the global minimum for elongation in fewer than 15 iterations for all three acquisition functions. In contrast, the random data acquisition failed to reach the optimum for yield and ultimate tensile strength but managed to reach the global minimum for elongation optimization at around 50 iterations.

Overall, all three acquisition functions performed better than the random acquisition function across all tasks for both computational and experimental datasets, with qPI being slightly worse than the other two. The reason for such underperformance is already discussed above, i.e., qPI only considers the improvement over the best-known materials and does not consider the relative improvement. Owing to this fact, PI often gets stuck in a local optima. In contrast, the qEI and qEHVI are very comparable, with qEI always performing slightly better at finding the global optimum within a minimal number of evaluations. Regarding computational cost, none of the three acquisition functions posed any significant bottleneck.

2-Dimensional Properties Optimization Results

Next, we explore the two-dimensional optimization profile for computational problems (refer to Figure 5). Focusing on novel materials discovery, which typically involves finding low-density materials with high heat capacity, thermal conductivity, and electrical conductivity, we aimed to minimize density while maximizing heat capacity, electrical conductivity, or thermal conductivity in two-dimensional optimizations. Additionally, we designed a problem to maximize heat capacity and thermal conductivity. In all four simulations, Bayesian Optimization (BO) outperformed random data acquisition, sometimes reaching the global maximum hypervolume within 50 iterations (starting with 25 seed points). To illustrate the quality of the acquired data points, we also present Pareto fronts for three runs with the best acquisition function identified in this work across three different optimization problems in Figure 7. As the objective was to maximize the hypervolume, the algorithm effectively identified points forming the basis of the Pareto front. However, extending the run duration or modifying the objective function could allow further exploration of specific regions in space, showcasing constrained BO as a potent tool.

In all three density minimization problems (with maximization of heat capacity, thermal conductivity, or electric conductivity), only qparEGO acquisition function performed poorly (only slightly better than random data acquisition); however, the other three, i.e., qEHVI, qNEHVI, and qNparEGO, showed impressive results, e.g., reaching the global maximum hypervolume within 20 for density minimization and heat capacity maximization problem. For the fourth problem, i.e., heat capacity and thermal conductivity maximization, all four acquisition functions, and random data acquisition performed exceptionally well, reaching $> 95\%$ hypervolume within 40 iterations. If we observe the one-dimensional optimization profile on the top panels of the associated subplots, it is quite evident that qparEGO, being a scalarization-based acquisition function, can comfortably optimize one of the objective functions, but falls short on the other objective function, which could be attributed to the poor choice of the scalarization function that most likely favored one objective over the other. Selection of suitable scalarization function is an active area of research. By taking the uncertainty into account, the parEGO formulation (qNparEGO) can perform as well as

EHVI-based methods, if not better. However, there is negligible performance difference between the qEHVI and its noisy variant (qNEHVI). It is of note that both the noisy variants, i.e., qNEHVI and qNparEGO required more time to compute the acquisition function values than their non-noisy counterparts. On average, they took 5-6 times more compute across all iterations (iteration time is smaller in the beginning of the simulations and slowly rises as we include more training samples to the active learning cycle).

For the experimental dataset, we maximized yield strength and ultimate tensile strength in one simulation, observing both the noisy variant performing quite well, with the qEHVI being very close to the maximum hypervolume and qparEGO being no better than the random data acquisition function. We maximized yield strength and ultimate tensile strength in two separate simulations while minimizing elongation. Although none reached the optimal point within our set 50 iterations, they achieved more than 90% of the maximum hypervolume within a budget of 50 experiments (excluding 25 seed points). Similar to the computational dataset, qparEGO performed very poorly, barely surpassing the random data acquisition function. In contrast, qEHVI, qNEHVI, and qNparEGO, all three, performed objectively better than the random data acquisition; however, qNEHVI turned out to be superior, owing to the fact that experimental data contains significant noise. The Pareto front for the simulation of minimization of elongation and maximization of ultimate tensile strength demonstrates its capability to identify almost all points on the global Pareto front. From this comparative analysis of computational and experimental datasets, it becomes evident that the qEHVI algorithm more readily identifies optima in the computational dataset with minimal computational cost, likely due to its noise-free nature. In contrast, qNEHVI performed better for the the experimental data optimization problems, owing to the fact that the data collected from experiments are subjected to conditions and measurement apparatus fluctuations, and likely contains more noise than the computational data.

3-Dimensional Properties Optimization Results

We also performed two 3-dimensional optimizations utilizing the computational dataset:

1. Density minimization along with heat capacity and electric conductivity maximization.
2. Density minimization along with heat capacity and thermal conductivity maximization.

Due to limited working computational memory (32 GB RAM), we could only run 40 iterations before hitting the working memory bottleneck. Similar to 2-dimensional optimization problems, both problems are satisfactorily optimized towards the global Pareto frontier by qEHVI, qNEHVI, and qNparEGO. Based on this analysis, given better computational resources, we can potentially optimize multi-objective problems involving objectives ($m \geq 3$) with this framework.

Multiple Data Acquisition Strategy

Finally, we also ran simulations where, instead of choosing one candidate point at each iteration, we chose multiple candidate points, e.g., two or four points, at each iteration. This could be preferable when limited time is available for exploration/exploitation, but facilities to run multiple experiments/computations are also available. By acquiring multiple candidate data points, the number of iterations is reduced significantly to reach a similar performance as a single data acquisition cycle. However, it scales sparingly; for instance, by acquiring two candidate points, one would not necessarily expect the number of iterations to be halved. In addition, owing to the intensive nature of Monte-Carlo simulations, we can only acquire 2 or 4 candidates successfully at each iteration before computational time and memory becomes an issue.

CONCLUSION

Developing rapid and reliable methods for multi-objective property optimization in materials science is essential in the era of the Materials Genome Initiative (MGI). In this context, we have demonstrated that q-expected hypervolume improvement (qEHVI), a hypervolume-based acquisition function, is highly effective for optimizing multi-component alloy systems with one-, two- and three-dimensional objectives. We also discovered that the Pareto frontier identified by this method after 50 iterations closely aligns with the global Pareto front. However, this model presupposes prior knowledge of the observations for candidate selection (discrete design space). In realistic scenarios, the necessary observations for candidate selection are often need to be made

available, or their acquisition requires simplifying assumptions about the search space. To address this limitation for numerical features, a more suitable approach would involve selecting candidates from a continuous search space. Furthermore, to render this optimization framework practically feasible, at least for simulations, computing the properties with on-the-fly computations after each iteration would be advantageous. We aim to make this framework user-friendly for discovering novel materials. To achieve this, we persistently adapting this method to a continuous search space with on-the-fly simulation capabilities. Additionally, we aim to encapsulate it in a user-friendly graphical user interface (GUI) for the materials science community in the near future. In conclusion, we can summarise the pivotal characteristics of this study:

- Singular efficiency in single-property optimization: Demonstrating remarkable efficiency, it identifies the optimal data within a dataset of Thirteen thousand instances in fewer than 75 evaluations.
- Multi-objective optimization prowess: For multi-objective optimization, our algorithm discerns a well-defined Pareto front within 70-75 iterations, closely aligned with the global Pareto front by achieving a hyper-volume of 90% to 100% of the maximum attainable.
- Enhanced candidate recommendation: It excels in recommending multiple candidates at each iteration, substantially expediting the discovery of novel alloys where parallel experimental or computational facilities are available.
- Rigorous construction of Surrogate model: Depending on the data quality and quantity, this framework discusses the best practices for constructing surrogate models that maximize the uncertainty quantification capability alongside minimizing computational cost.

DATA AND CODE AVAILABILITY STATEMENT

The code is available at <https://github.com/mamunm/AlloyOpt>. Trained Bayesian optimisation (BO) processes based on Active Learning (AL) principles, and the data underpinning the conclusions of this study, are accessible from the corresponding author upon a reasonable request.

REFERENCES

- Agrawal, A. and Choudhary, A. (2016). “Perspective: Materials informatics and big data: Realization of the “fourth paradigm” of science in materials science.” *Apl Materials*, 4(5).
- Balandat, M., Karrer, B., Jiang, D. R., Daulton, S., Letham, B., Wilson, A. G., and Bakshy, E. (2020). “BoTorch: A Framework for Efficient Monte-Carlo Bayesian Optimization.” *Advances in Neural Information Processing Systems* 33, <<http://arxiv.org/abs/1910.06403>>.
- Bradford, E., Schweidtmann, A. M., and Lapkin, A. (2018). “Efficient multiobjective optimization employing gaussian processes, spectral sampling and a genetic algorithm.” *Journal of global optimization*, 71(2), 407–438.
- Cantor, B. (2014). “Multicomponent and high entropy alloys.” *Entropy*, 16(9), 4749–4768.
- Daulton, S., Balandat, M., and Bakshy, E. (2020). “Differentiable expected hypervolume improvement for parallel multi-objective bayesian optimization.” *Advances in Neural Information Processing Systems*, 33, 9851–9864.
- Daulton, S., Balandat, M., and Bakshy, E. (2021). “Parallel bayesian optimization of multiple noisy objectives with expected hypervolume improvement.” *Advances in Neural Information Processing Systems*, 34, 2187–2200.
- Eriksson, D. and Jankowiak, M. (2021). “High-dimensional bayesian optimization with sparse axis-aligned subspaces.” *Uncertainty in Artificial Intelligence*, PMLR, 493–503.
- Frazier, P. (2018). “A tutorial on bayesian optimization.” *ArXiv*, abs/1807.02811.
- Gardner, J. R., Pleiss, G., Bindel, D., Weinberger, K. Q., and Wilson, A. G. (2018). “Gpytorch: Blackbox matrix-matrix gaussian process inference with gpu acceleration.” *Advances in Neural Information Processing Systems*.
- Gebhardt, T., Music, D., Takahashi, T., and Schneider, J. M. (2012). “Combinatorial thin film materials science: From alloy discovery and optimization to alloy design.” *Thin Solid Films*, 520(17), 5491–5499.

- Hupkens, I., Deutz, A., Yang, K., and Emmerich, M. (2015). “Faster exact algorithms for computing expected hypervolume improvement.” *international conference on evolutionary multi-criterion optimization*, Springer, 65–79.
- Khatamsaz, D., Vela, B., Singh, P., Johnson, D. D., Allaire, D., and Arróyave, R. (2023). “Bayesian optimization with active learning of design constraints using an entropy-based approach.” *npj Computational Materials*, 9(1), 49.
- Knowles, J. (2006). “Parego: A hybrid algorithm with on-line landscape approximation for expensive multiobjective optimization problems.” *IEEE transactions on evolutionary computation*, 10(1), 50–66.
- Liang, Q., Gongora, A. E., Ren, Z., Tiihonen, A., Liu, Z., Sun, S., Deneault, J. R., Bash, D., Mekki-Berrada, F., Khan, S. A., et al. (2021). “Benchmarking the performance of bayesian optimization across multiple experimental materials science domains.” *npj Computational Materials*, 7(1), 188.
- Liu, X., Zhang, J., and Pei, Z. (2023). “Machine learning for high-entropy alloys: progress, challenges and opportunities.” *Progress in Materials Science*, 131, 101018.
- Long, H., Mao, S., Liu, Y., Zhang, Z., and Han, X. (2018). “Microstructural and compositional design of ni-based single crystalline superalloys—a review.” *Journal of Alloys and Compounds*, 743, 203–220.
- Mamun, O., Taufique, M., Wenzlick, M., Hawk, J., and Devanathan, R. (2022). “Uncertainty quantification for bayesian active learning in rupture life prediction of ferritic steels.” *Scientific Reports*, 12(1), 2083.
- Mamun, O., Wenzlick, M., Hawk, J., and Devanathan, R. (2021). “A machine learning aided interpretable model for rupture strength prediction in fe-based martensitic and austenitic alloys.” *Scientific Reports*, 11(1), 5466.

- Pedregosa, F., Varoquaux, G., Gramfort, A., Michel, V., Thirion, B., Grisel, O., Blondel, M., Prettenhofer, P., Weiss, R., Dubourg, V., Vanderplas, J., Passos, A., Cournapeau, D., Brucher, M., Perrot, M., and Duchesnay, E. (2011). “Scikit-learn: Machine learning in Python.” *Journal of Machine Learning Research*, 12, 2825–2830.
- Pfeiffer, O. P., Liu, H., Montanelli, L., Latypov, M. I., Sen, F. G., Hegadekatte, V., Olivetti, E. A., and Homer, E. R. (2022). “Aluminum alloy compositions and properties extracted from a corpus of scientific manuscripts and us patents.” *Scientific Data - Nature*, 9(128).
- Shahriari, B., Swersky, K., Wang, Z., Adams, R. P., and de Freitas, N. (2016). “Taking the human out of the loop: A review of bayesian optimization.” *Proceedings of the IEEE*, 104(1), 148–175.
- Snoek, J., Larochelle, H., and Adams, R. P. (2012). “Practical bayesian optimization of machine learning algorithms.” *Advances in neural information processing systems*, 25.
- Virtanen, P., Gommers, R., Oliphant, T. E., Haberland, M., Reddy, T., Cournapeau, D., Burovski, E., Peterson, P., Weckesser, W., Bright, J., van der Walt, S. J., Brett, M., Wilson, J., Millman, K. J., Mayorov, N., Nelson, A. R. J., Jones, E., Kern, R., Larson, E., Carey, C. J., Polat, İ., Feng, Y., Moore, E. W., VanderPlas, J., Laxalde, D., Perktold, J., Cimrman, R., Henriksen, I., Quintero, E. A., Harris, C. R., Archibald, A. M., Ribeiro, A. H., Pedregosa, F., van Mulbregt, P., and SciPy 1.0 Contributors (2020). “SciPy 1.0: Fundamental Algorithms for Scientific Computing in Python.” *Nature Methods*, 17, 261–272.
- Zhan, X., Liu, H., Li, Q., and Chan, A. B. (2021). “A comparative survey: Benchmarking for pool-based active learning.” *IJCAI*, 4679–4686.

List of Figures

1	The workflow to train multi-objective Bayesian active learning framework for alloy properties optimization	26
2	Comperative barplot of different GP model implementations. The top panel illustrates the R^2 value on the test set, the middle panel shows the coverage, and the third panel shows the time taken to train the model on a natural log scale (on a 13th Gen Intel® Core™ i7-13700HX processor with 32 GB ram memory). We also show a black dotted line in the middle panel to indicate the 95% coverage line to compare the quality of the uncertainty quantification capabilities of different GP model implementations.	27
3	Optimization profiles for 1-dimensional optimization of the computational properties with four different acquisition algorithms, i.e., qEHVI, qEI, qPI, and random. These profiles are generated using the average of five different runs with 25 initial random seed points.	28
4	Optimization profiles for 1-dimensional optimization of the experimental properties with four different acquisition algorithms, i.e., qEHVI, qEI, qPI, and random. These profiles are generated using the average of five different runs with 25 initial random seed points.	29
5	Optimization profiles for 2-dimensional optimization of the computational properties with five different acquisition algorithms, i.e., qEHVI, qNEHVI, qparEGO, qNparEGO, and random. In each subfigures, the top two panel shows the optimization profile of the two properties during the multiobjective optimization run, while the third panel shows the hypervolume optimization profile. These profiles are generated using the average of five different runs with 25 initial random seed points.	30

- 6 Optimization profiles for 2-dimensional optimization of the experimental properties with five different acquisition algorithms, i.e., qEHVI, qNEHVI, qparEGO, qNparEGO, and random. In each subfigures, the top two panel shows the optimization profile of the two properties during the multiobjective optimization run, while the third panel shows the hypervolume optimization profile. These profiles are generated using the average of five different runs with 25 initial random seed points. 31
- 7 Pareto front of the selected runs for some selected 2-dimensional optimization. The global Pareto front is shown as a teal line while the Pareto front obtained at the end of the simulations is shown as a red marker (★). The black squares represent all the data in the database (a) Density Minimization and Electrical Conductivity Maximization, (b) Density Minimization and Thermal Conductivity Maximization, and (c) Elongation Minimization and Ultimate Tensile Strength Maximization. For computational data ((a) & (b)), we use qEHVI, and for experimental data ((c)), we use qNEHVI. 32
- 8 Optimization profiles for 3-dimensional optimization of the computational properties with five different acquisition algorithms, i.e., qEHVI, qNEHVI, qparEGO, qNparEGO, and random. In each subfigures, the top three panel shows the optimization profile of the three properties during the multiobjective optimization run, while the fourth panel shows the hypervolume optimization profile. These profiles are generated using the average of five different runs with 25 initial random seed points. 33

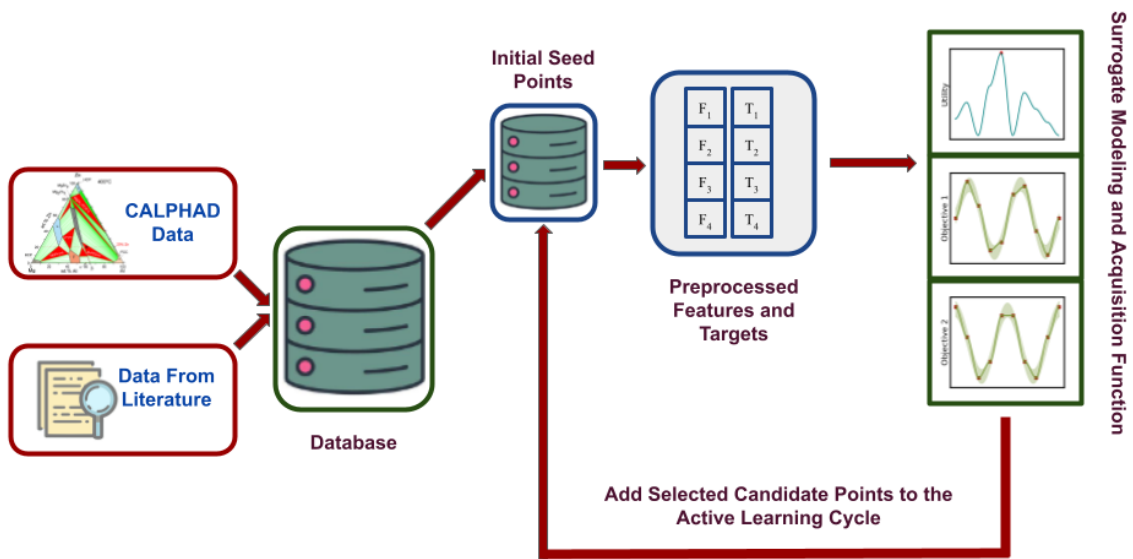


Fig. 1. The workflow to train multi-objective Bayesian active learning framework for alloy properties optimization

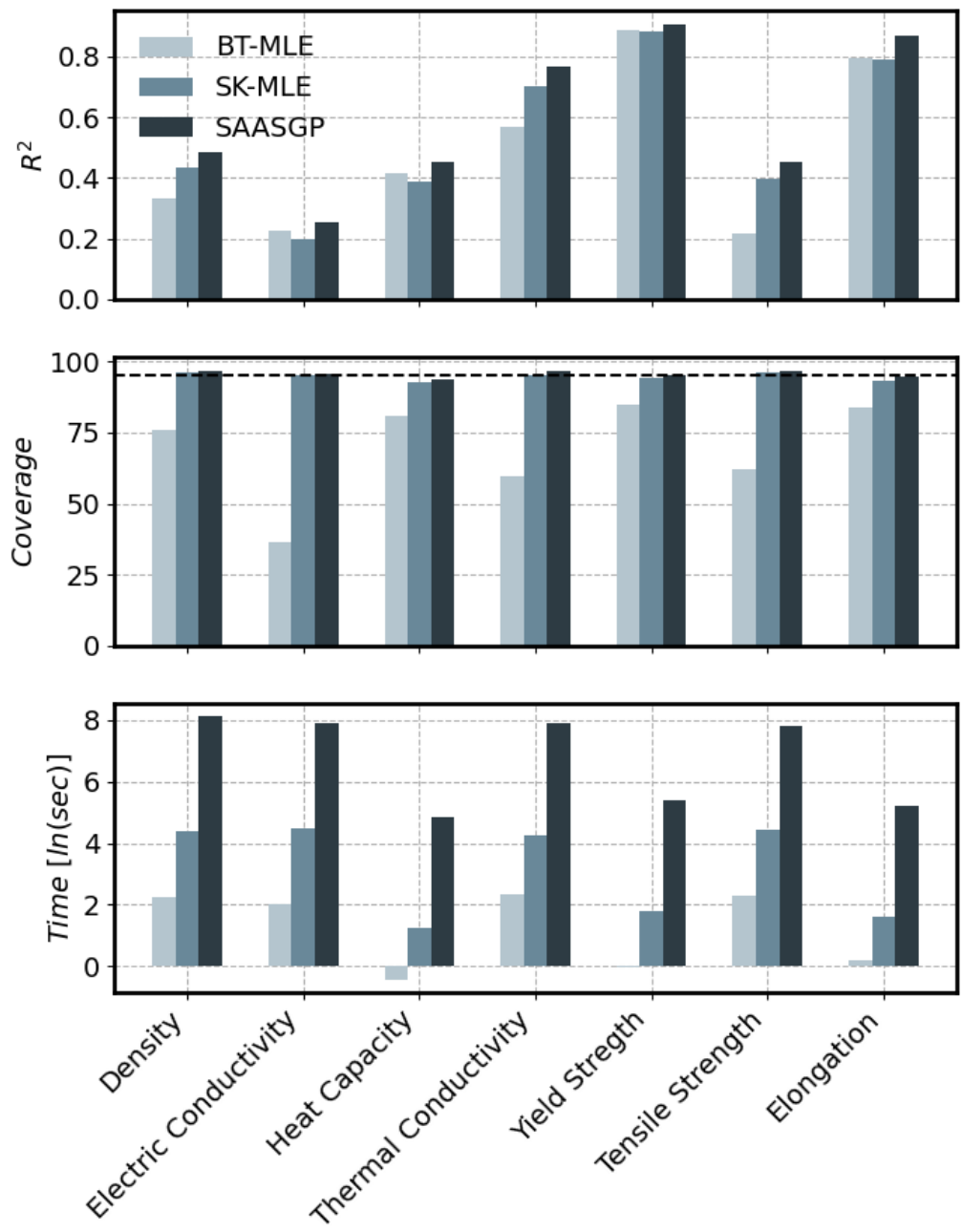
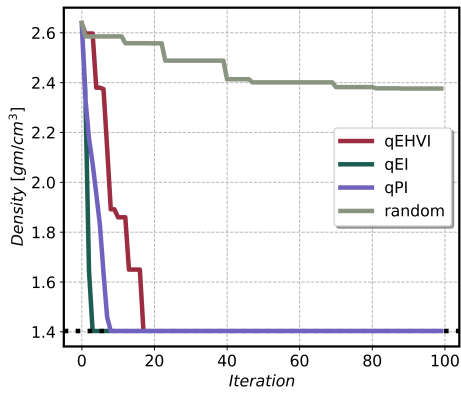
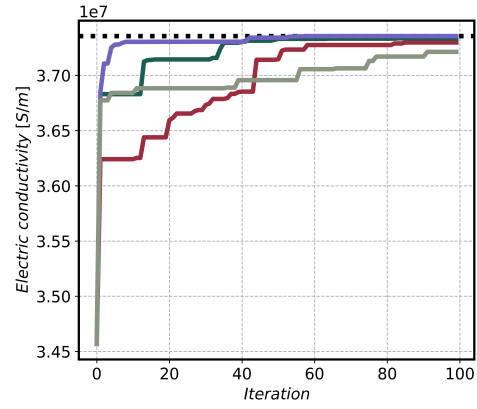


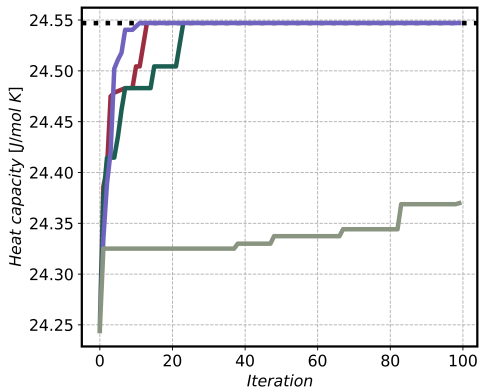
Fig. 2. Comparative barplot of different GP model implementations. The top panel illustrates the R^2 value on the test set, the middle panel shows the coverage, and the third panel shows the time taken to train the model on a natural log scale (on a 13th Gen Intel® Core™ i7-13700HX processor with 32 GB ram memory). We also show a black dotted line in the middle panel to indicate the 95% coverage line to compare the quality of the uncertainty quantification capabilities of different GP model implementations.



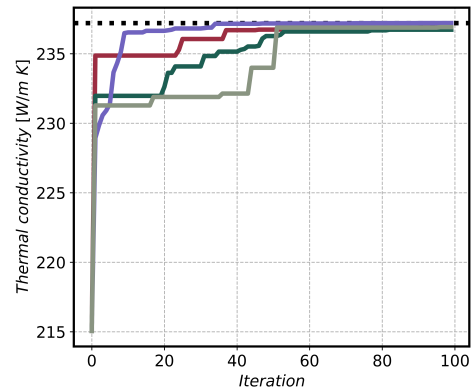
(a) Density Minimization



(b) Electric Conductivity Maximization

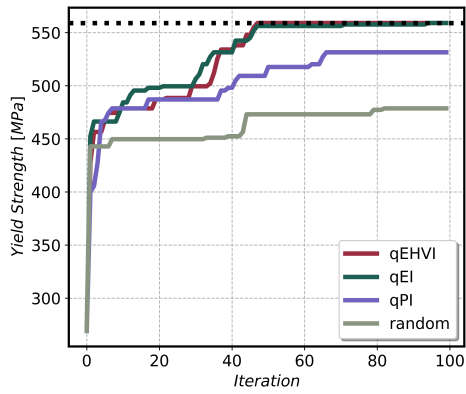


(c) Heat Capacity Maximization

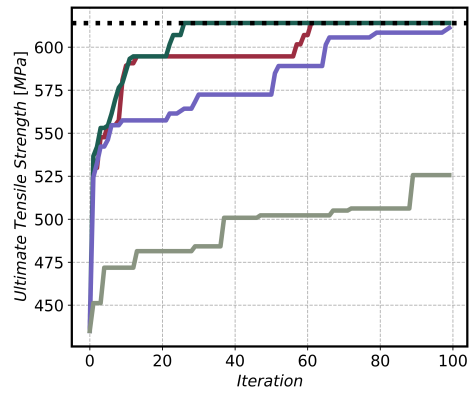


(d) Thermal Conductivity Maximization

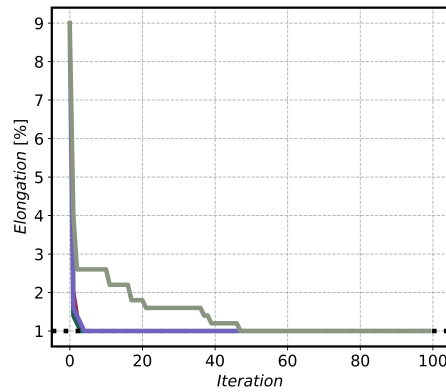
Fig. 3. Optimization profiles for 1-dimensional optimization of the computational properties with four different acquisition algorithms, i.e., qEHVI, qEI, qPI, and random. These profiles are generated using the average of five different runs with 25 initial random seed points.



(a) Yield Strength Maximization

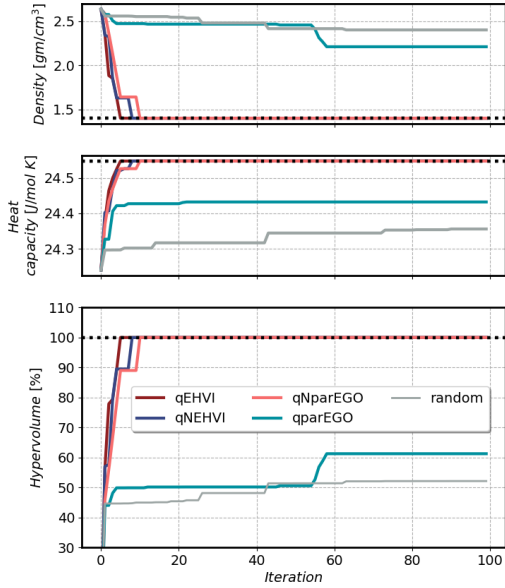


(b) Ultimate Tensile Strength Maximization

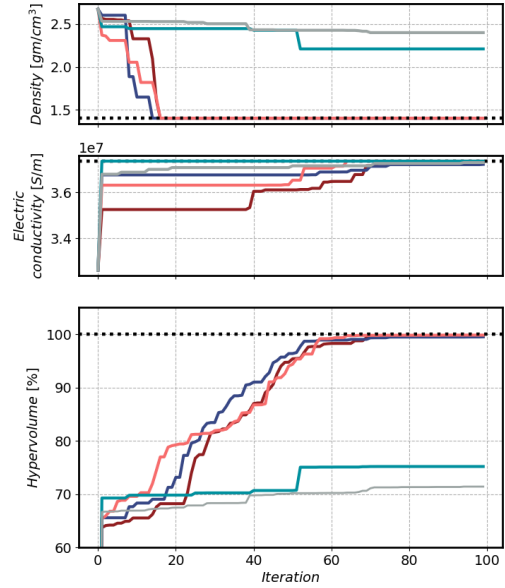


(c) Elongation Minimization

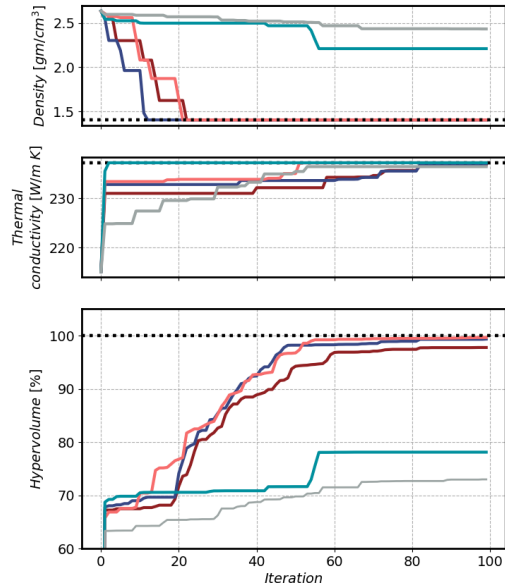
Fig. 4. Optimization profiles for 1-dimensional optimization of the experimental properties with four different acquisition algorithms, i.e., qEHVI, qEI, qPI, and random. These profiles are generated using the average of five different runs with 25 initial random seed points.



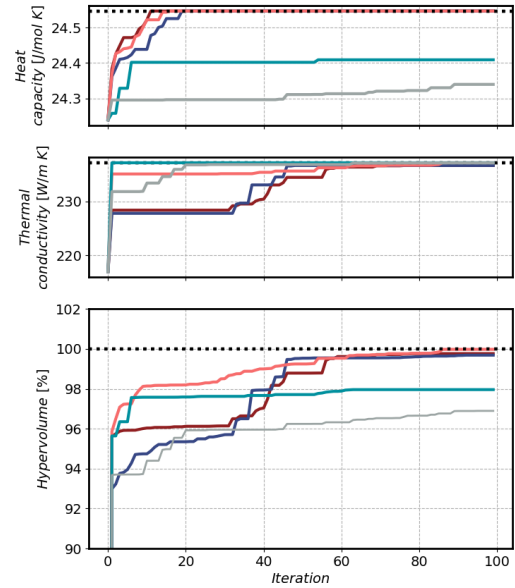
(a) Density Minimization and Heat Capacity Maximization



(b) Density Minimization and Electric Conductivity Maximization



(c) Density Minimization and Thermal Conductivity Maximization



(d) Heat Capacity and Thermal Conductivity Maximization

Fig. 5. Optimization profiles for 2-dimensional optimization of the computational properties with five different acquisition algorithms, i.e., qEHVI, qNEHVI, qparEGO, qNparEGO, and random. In each subfigures, the top two panel shows the optimization profile of the two properties during the multiobjective optimization run, while the third panel shows the hypervolume optimization profile. These profiles are generated using the average of five different runs with 25 initial random seed points.

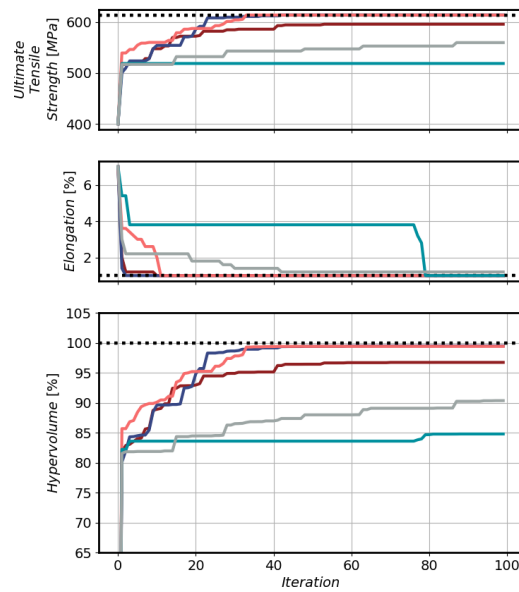
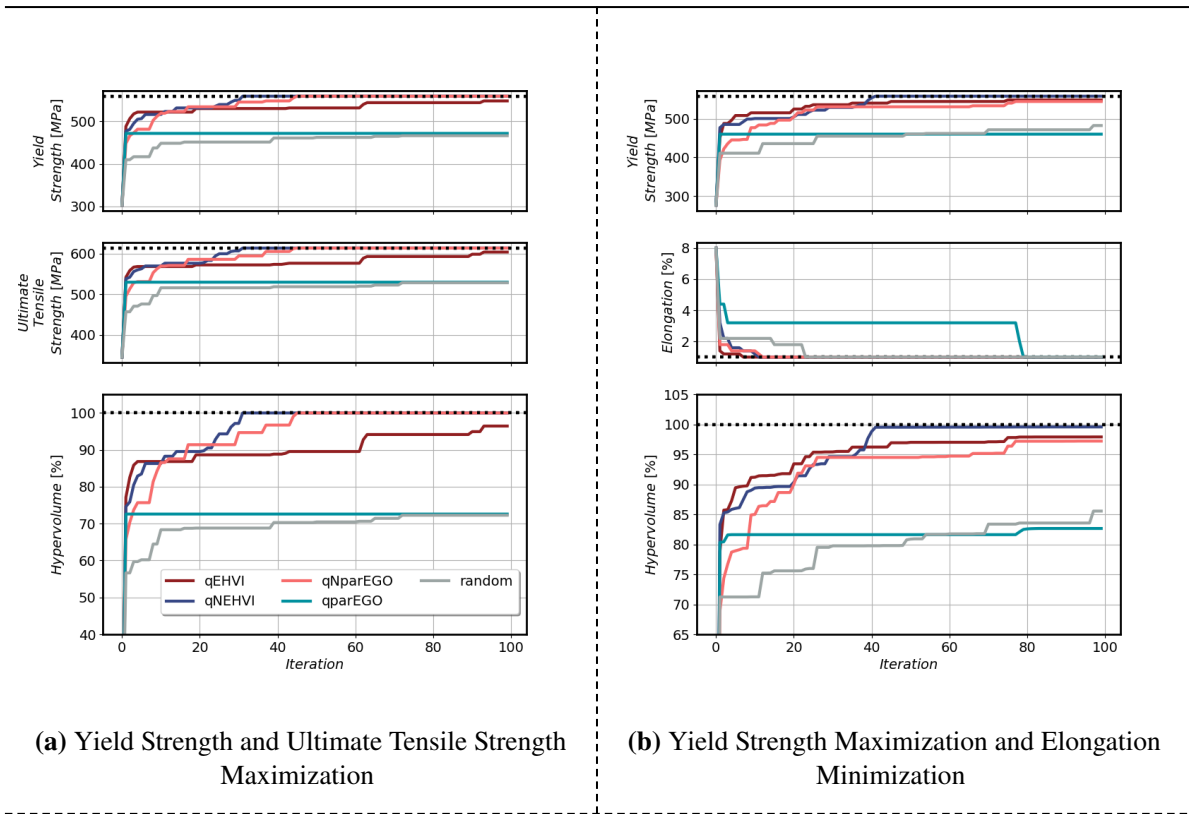
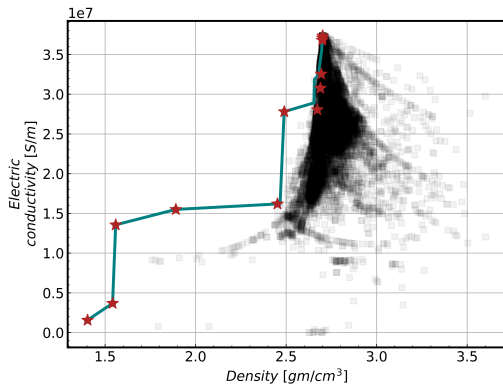
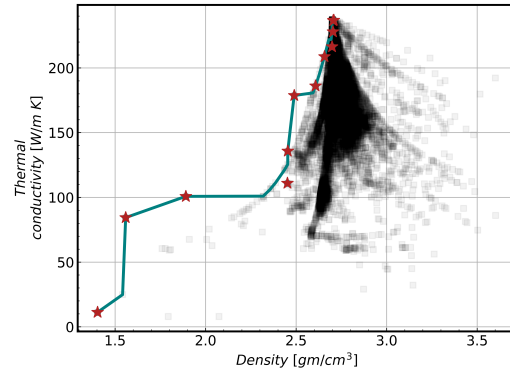


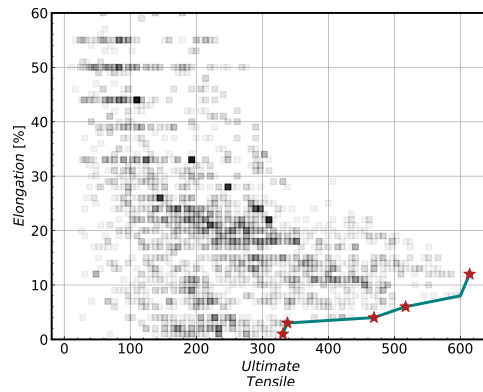
Fig. 6. Optimization profiles for 2-dimensional optimization of the experimental properties with five different acquisition algorithms, i.e., qEHVI, qNEHVI, qparEGO, qNparEGO, and random. In each subfigures, the top two panel shows the optimization profile of the two properties during the multiobjective optimization run, while the third panel shows the hypervolume optimization profile. These profiles are generated using the average of five different runs with 25 initial random seed points.



(a) Density Minimization and Electrical Conductivity Maximisation

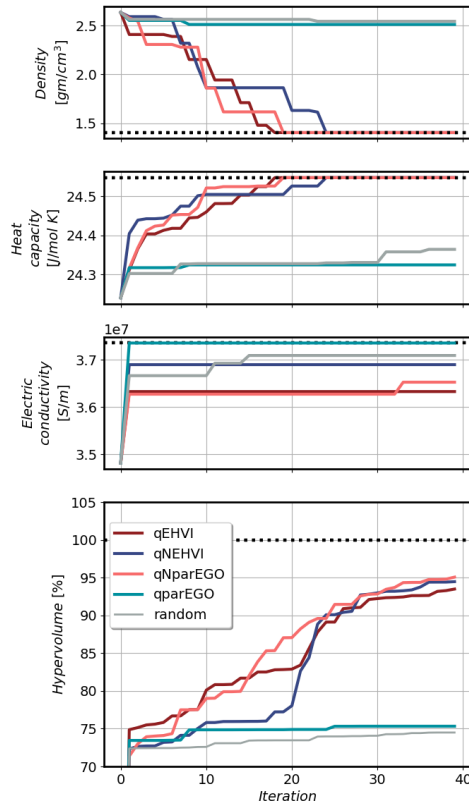


(b) Density Minimization and Thermal Conductivity Maximisation

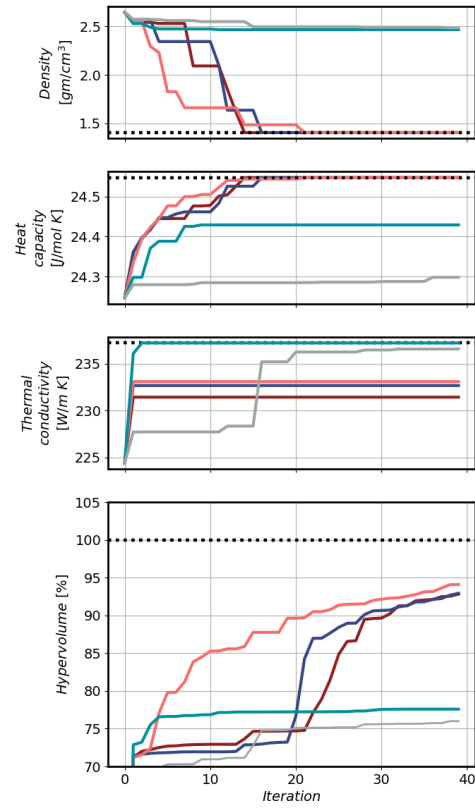


(c) Ultimate Tensile Strength Maximization and Elongation Minimization

Fig. 7. Pareto front of the selected runs for some selected 2-dimensional optimization. The global Pareto front is shown as a teal line while the Pareto front obtained at the end of the simulations is shown as a red marker (★). The black squares represent all the data in the database (a) Density Minimization and Electrical Conductivity Maximization, (b) Density Minimization and Thermal Conductivity Maximization, and (c) Elongation Minimization and Ultimate Tensile Strength Maximization. For computational data ((a) & (b)), we use qEHVI, and for experimental data ((c)), we use qNEHVI.



(a) Density Minimization and Heat Capacity & Electric Conductivity Maximization



(b) Density Minimization and Heat Capacity & Thermal Conductivity Maximization

Fig. 8. Optimization profiles for 3-dimensional optimization of the computational properties with five different acquisition algorithms, i.e., qEHVI, qNEHVI, qparEGO, qNparEGO, and random.

In each subfigures, the top three panel shows the optimization profile of the three properties during the multiobjective optimization run, while the fourth panel shows the hypervolume optimization profile. These profiles are generated using the average of five different runs with 25 initial random seed points.

Supporting Documents for Accelerated Development of Multi-component Alloys in Discrete Design Space Using Bayesian Multi-Objective Optimization

Osman Mamun¹, Markus Bause², and Bhuiyan Shameem Mahmood Ebna Hai^{1,2,*}

¹Fehrmann MaterialsX GmbH - Fehrmann Tech Group, Hamburg, Germany

²Helmut Schmidt University - University of the Federal Armed Forces Hamburg, Germany

*Corresponding author: shameem.ebna.hai@fehrmann-materials.com

APPENDIX A

Supporting Figure 1 displays a histogram illustrating the distribution of target properties in the computational data. In Supporting Figure 2, we illustrate a 2D projection of the high-dimensional composition space for aluminium alloys from computational data with the assistance of the t-Stochastic Neighbor Embedding (tSNE) plot. Here, the aluminium alloys are classified into distinct series based on their composition: the 1xxx series primarily composed of at least 99% aluminium; the 2xxx series featuring copper as the principal alloying element; the 3xxx series characterised by manganese as the primary alloying component; the 4xxx series, where silicon serves as the primary alloying agent; the 5xxx series distinguished by magnesium as the main alloying element; the 6xxx series comprising silicon and magnesium as the primary alloying elements; the 7xxx series characterised by zinc as the primary alloying element, alongside magnesium and copper; and finally, the 8xxx series encompassing miscellaneous aluminium alloys not classified within the preceding series. The colour of the points in Figure 2 indicates crucial alloy composition information for aluminium alloys derived from computational data, where the colour corresponds to the alloy series (1xxx is blue, 2xxx is dark yellow, 3xxx is green, 4xxx is orange, 5xxx is purple, 6xxx is brown, 7xxx is pink, and 8xxx is grey). Furthermore, in Supporting Figure 3, we present

a violin plot to demonstrate the distribution of computational material properties (e.g., density, electrical conductivity, heat capacity, and thermal conductivity), categorised by the alloy series.

APPENDIX B

Supporting Figure 4 shows a histogram illustrating the distribution of these target properties in the experimental data. Supporting Figures 5 and 6, respectively, depict a 2D projection of the high-dimensional feature space for aluminium alloys from experimental data using the tSNE plot and a violin plot illustrating the distribution of the experimental material properties (e.g., yield stress, ultimate tensile stress, and elongation), categorised by the alloy series.

List of Figures

1 Target property distribution of the computational dataset. (a) Density, (b) Electrical Conductivity, (c) Heat Capacity, and (d) Thermal Conductivity 4

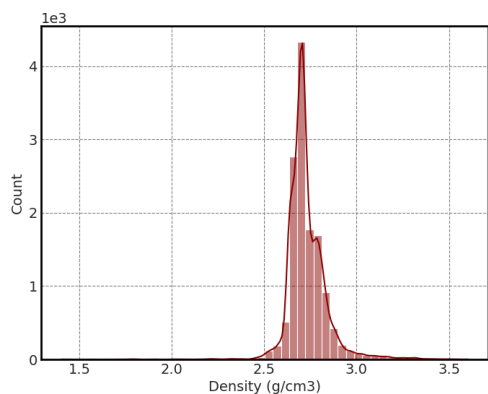
2 The t-Stochastic Neighbor Embedding (tSNE) illustrates the distribution of the computational data in the two-dimensional latent space. Different colours indicate the chemical composition of various series of aluminium alloy materials. 5

3 Material Property Distribution in the Computational Dataset. Various colours represent distinct classes of Aluminium alloy materials. The violin plot displays the distribution of (a) Density, (b) Electrical Conductivity, (c) Heat Capacity, and (d) Thermal Conductivity, categorized by the alloy series. 6

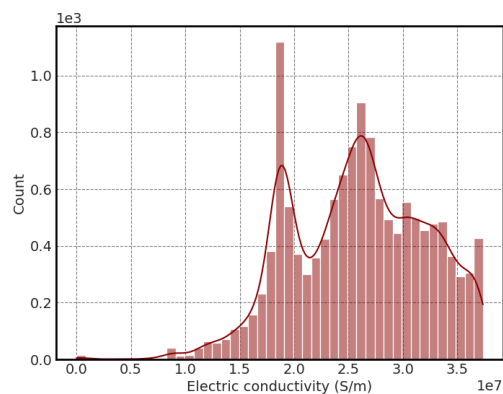
4 Target property distribution of the experimental dataset. (a) Yield Strength, (b) Ultimate Tensile Strength, and (c) Elongation 7

5 The t-Stochastic Neighbor Embedding (tSNE) illustrates the distribution of various data instances projected on a 2D plane from the experimental data. Different colours indicate the chemical composition of different series of aluminium alloy materials. 8

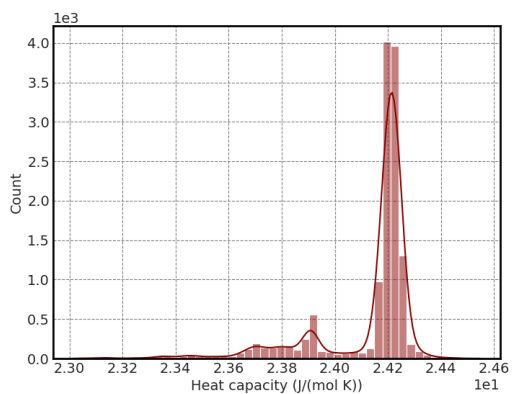
6 Distribution of Mechanical Properties in the Experimental Dataset: Different colours indicate distinct classes of aluminium alloy materials. The violin plot showcases the distribution of (a) Yield Strength, (b) Ultimate Tensile Strength, and (c) Elongation, classified by the alloy series. 9



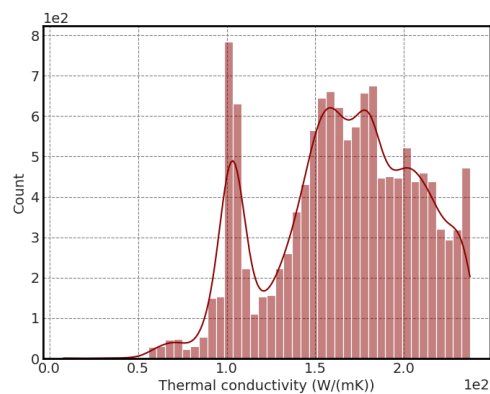
(a) Density



(b) Electrical Conductivity

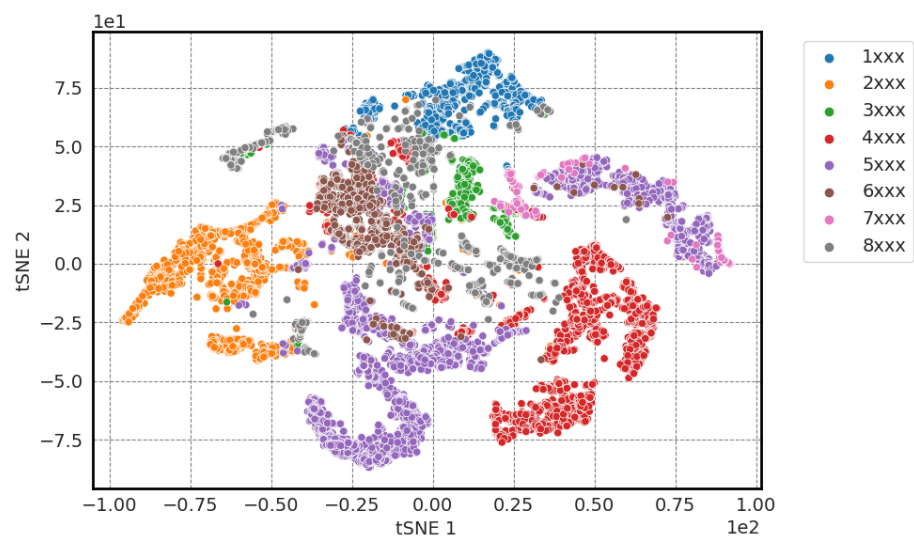


(c) Heat Capacity

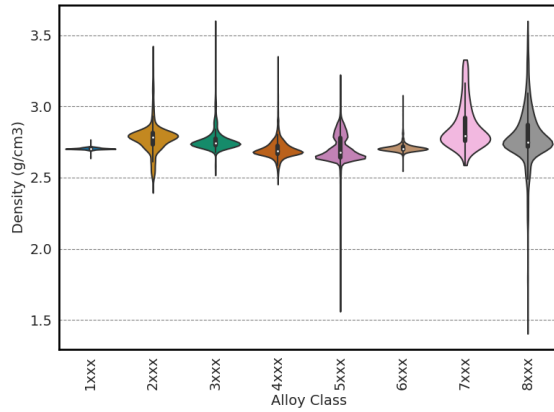


(d) Thermal Conductivity

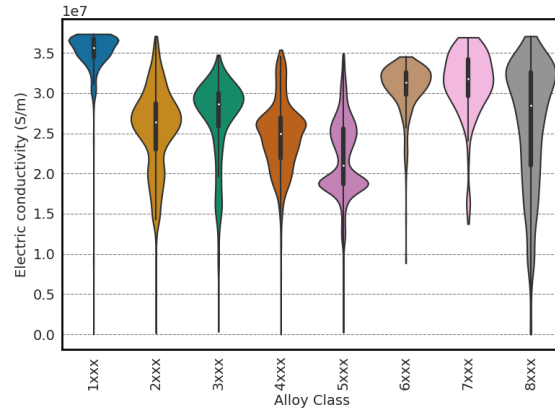
Supporting Figure 1. Target property distribution of the computational dataset. (a) Density, (b) Electrical Conductivity, (c) Heat Capacity, and (d) Thermal Conductivity



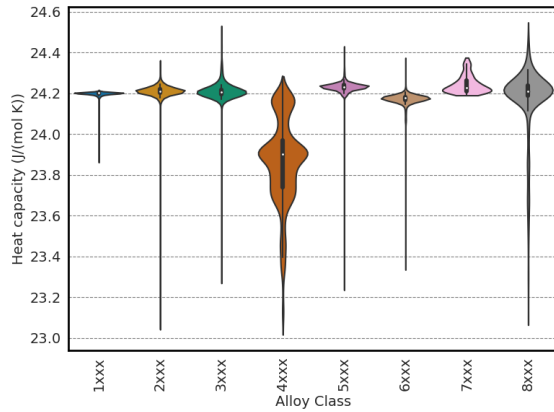
Supporting Figure 2. The t-Stochastic Neighbor Embedding (tSNE) illustrates the distribution of the computational data in the two-dimensional latent space. Different colours indicate the chemical composition of various series of aluminium alloy materials.



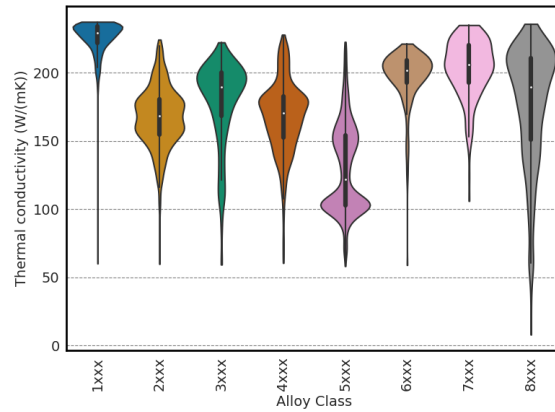
(a) Density



(b) Electrical Conductivity

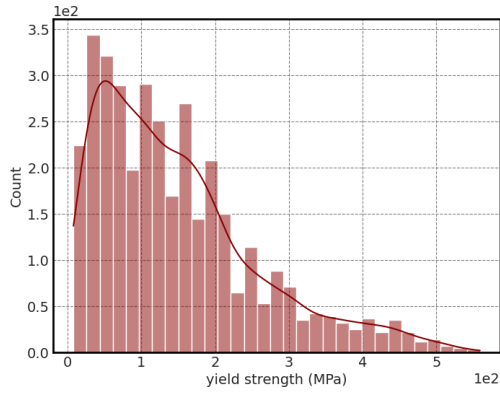


(c) Heat Capacity

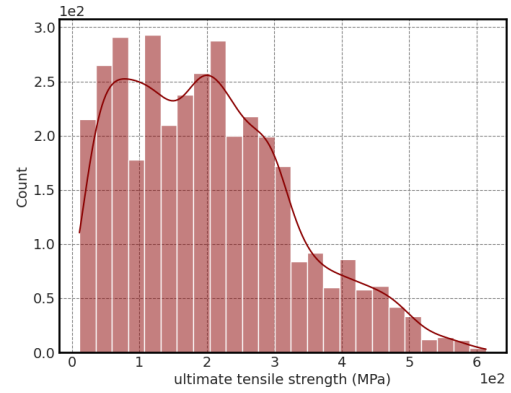


(d) Thermal Conductivity

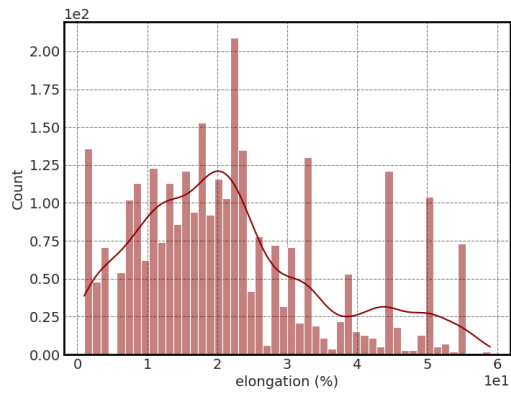
Supporting Figure 3. Material Property Distribution in the Computational Dataset. Various colours represent distinct classes of Aluminium alloy materials. The violin plot displays the distribution of (a) Density, (b) Electrical Conductivity, (c) Heat Capacity, and (d) Thermal Conductivity, categorized by the alloy series.



(a) Yield Strength

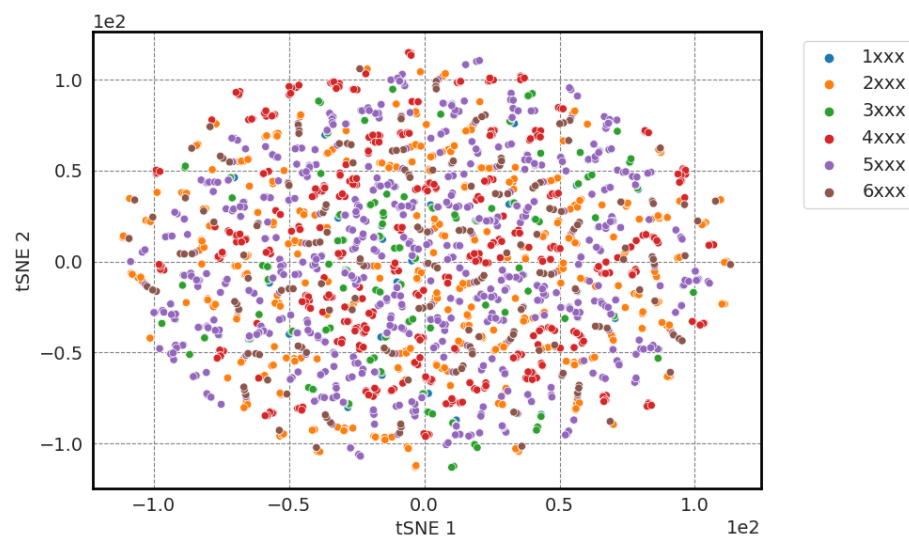


(b) Ultimate Tensile Strength

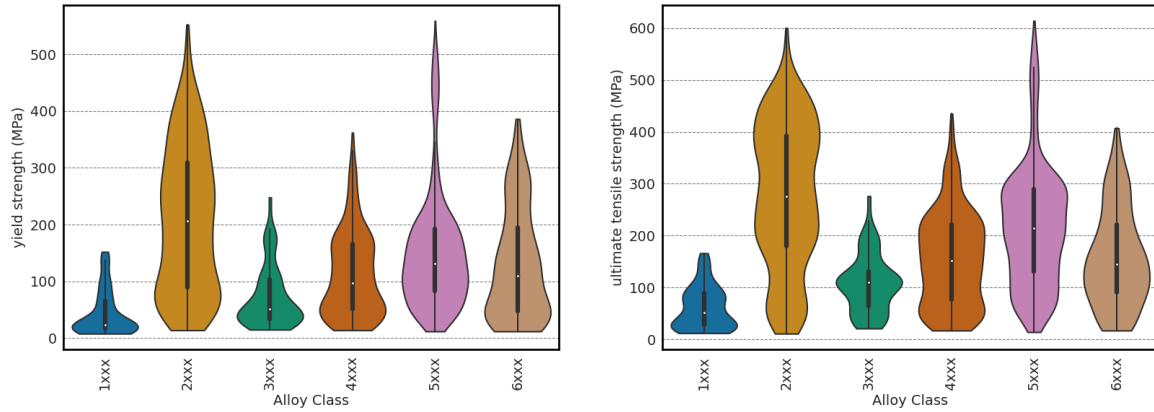


(c) Elongation

Supporting Figure 4. Target property distribution of the experimental dataset. (a) Yield Strength, (b) Ultimate Tensile Strength, and (c) Elongation

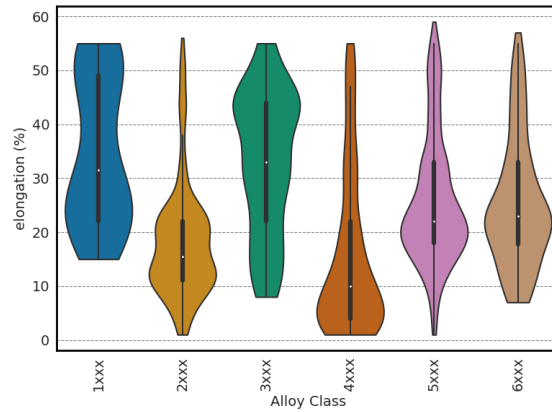


Supporting Figure 5. The t-Stochastic Neighbor Embedding (tSNE) illustrates the distribution of various data instances projected on a 2D plane from the experimental data. Different colours indicate the chemical composition of different series of aluminium alloy materials.



(a) Yield Strength

(b) Ultimate Tensile Strength



(c) Elongation

Supporting Figure 6. Distribution of Mechanical Properties in the Experimental Dataset: Different colours indicate distinct classes of aluminium alloy materials. The violin plot showcases the distribution of (a) Yield Strength, (b) Ultimate Tensile Strength, and (c) Elongation, classified by the alloy series.